

Confined spin-wave characteristics in magnetic nanowire ensembles approaching the ultrathin regime

Abhijit Ghosh,^{1,*} Abhishek Talapatra², Sarjoosing Goolaup,^{1,3} and Sze Ter Lim^{1,†}

¹*Institute of Materials Research and Engineering, A*STAR, 2 Fusionopolis Way, #08-03 Innovis, Singapore 138634, Singapore*

²*Department of Applied Physics, Aalto University, Espoo 02150, Finland*

³*School of Engineering and Innovation, The Open University, Milton Keynes, MK7 6AA, United Kingdom*

(Received 25 March 2022; revised 18 July 2023; accepted 4 August 2023; published 12 October 2023)

We present a comprehensive study on the high-frequency magnetization dynamics of homogeneously patterned ultrathin magnetic nanowire arrays. The backward volume magnetostatic spin-wave (BVMSW) and Damon-Eshbach (DE) configurations are studied along with the intermediate transition states to understand the edge mode's evolution in depth. We find at the sub-10-nm ultrathin regime the dynamics are heavily influenced by geometrical parameters such as magnetic layer thickness (t_{FM}), demagnetization factors, and interfaces. Critical entities such as field separation δH between uniform to edge mode increase linearly with $1/t_{\text{FM}}$, while the edge saturation field $H_{\text{sat}}^{\text{edge}}$ increase monotonically with increasing t_{FM} , revealing excellent agreement between findings from experimental and micromagnetic simulations. The dynamics are less sensitive to the width of the nanowire but very sensitive to the adjacent material or the interface of the ferromagnet, especially at the ultrathin limits.

DOI: [10.1103/PhysRevApplied.20.044034](https://doi.org/10.1103/PhysRevApplied.20.044034)

I. INTRODUCTION

The prospects of spin-wave- (SW) based information processing and transmission in the gigahertz and subterahertz frequency regime rely heavily on efficient propagation, tuning and control of spin waves [1–3]. Spin-wave studies using metamaterials have shown that the SW characteristics can be tailored using sample geometry [4,5], applied field [6], reconfigurability of magnetic textures [7], and by propagation direction [8]. Periodic arrays of magnetic nanowires (NWs) are amongst the most studied metamaterials, both in conventional [9–11] and unconventional [12,13] forms. Although yttrium iron garnet (YIG), due to its low damping [14,15], was considered the most suitable material for SW-based applications, its growth-related concerns have motivated researchers to look for industry-friendly solutions in common spintronic metals [9,16,17]. One caveat with the recent experimental studies has been the use of relatively thick ferromagnetic layers in the 10's nm regime [10,18,19]. With conventional spintronics devices reaching sub-10-nm limits and the advent of interfacial and spin-orbital effects [20,21], there is a need to explore spin-wave characteristics at ultrathin limits to probe the spin-wave quantization and confinement and their geometrical dependencies.

It is seen that standing-spin-wave resonances in magnetic wires and patterned arrays could form dispersionless modes due to spin-wave quantization along the direction of lateral confinement [22,23]. Besides, such confinement can give rise to additional excitation, which is primarily contributed by the magnetization at the nanostructures' edges. Recent findings [24,25] reveal that strong coupling in the magnonic cavity is attractive for the study of cavity quantum electrodynamics utilizing magnons. Nevertheless, several unexplored domains related to magnonic confinement in traditional magnetic metamaterials, such as nanowire ensembles, are still present, which could help answer fundamental questions related to spin waves. Exploring those unknown and less-explored domains is the primary motivation for this present work. This work presents a comprehensive study of spin-wave dynamics and confinement in nanowire ensembles. Key factors that govern spin-wave propagation and confinement [26], such as the angle of the applied field with respect to the NW axis, individual nanowire width, the thickness of the layer subjected to resonance excitation, and composition of the heterostructure, are probed in greater detail. Moreover, we have emphasized carrying out independent but corroborative studies using experiments and micromagnetic simulations. We primarily focus on the ultrathin ferromagnetic limits where the interplay of different demagnetization factors and the anisotropic field becomes critical in governing the characteristics and features of the nanowire dynamics. Further,

*abhijit.phy@gmail.com

†lim_sze_ter@imre.a-star.edu.sg

the capability of tuning and controlling the dynamic characteristics can contribute towards spin-wave-based device design [1].

II. METHODS

A. Growth and fabrication

A series of $\text{Co}_{20}\text{Fe}_{60}\text{B}_{20}$ (CFB) based thin films in the range of 1.4 to 7.5 nm, with excellent thickness control, were deposited on ion-cleaned Si/SiO₂ substrates using ultrahigh vacuum magnetron sputtering, under a base pressure of $<5 \times 10^{-8}$ mbar and 3 mbar of Ar⁺ environment. 5-nm-thick *W* underlayer and 2-nm-thick MgO capping was used for most of the samples. For studying the impact of adjacent metals of the FM layer (heavy and light) in the dynamic characteristics of the nanowire ensembles, a different series of samples were grown using various combinations of underlayer (W, Pt, Cu, MgO), and overlayer materials. For nanowire fabrication, electron-beam lithography, using *ma-N* 2403 photoresist, and *ma-D* 525 developer was used, followed by chemically assisted ion-beam etching over a considerably large area (approximately $2 \times 2 \text{ mm}^2$) to develop compatibility with our waveguide used in the inductive ferromagnetic resonance tool. A critical etching angle to minimize the shadowing effect (as well as redeposition), which is very common for these types of dense nanostructure fabrication processes and the feedback from SEM images, was used to optimize the critical etch conditions. A typical SEM image of our representative sample is presented in Fig. 1(a), which depicts the enlarged view of our sample. The characteristic width (*w*) (light gray region) of the individual NW is set approximately at 125 nm, respectively, with a similar gap (*g*) (dark gray region) between successive NWs [Fig. 1(a)], while the lengths of the nanowires are 2 μm . The consideration of *w* = *g* reduces the interwire magnetostatic interaction and hence ensures that the structures' shape anisotropy governs the magnetic phenomena. The relative orientation of the applied field *H* with respect to the easy axis (EA) and hard axes (HA) of the NWs are alongside the corresponding demagnetizing factors of *N_x*, *N_y*, and *N_z* are indicated in Fig. 1(a).

B. Experimental characterizations

The magnetometry studies of the films and a few nanowire ensembles were performed by a superconducting quantum interference device (SQUID) magnetometer. The magnetization dynamics studies were performed using a homebuilt broadband FMR spectrometer in fixed-frequency field sweep mode [27]. The samples were mounted on a nonmagnetic sample holder capable of precise rotation with small inaccuracy [28]. The microwave field *h*^{rf} was transmitted through a coplanar waveguide (CPW) on top of which the magnetic sample was placed

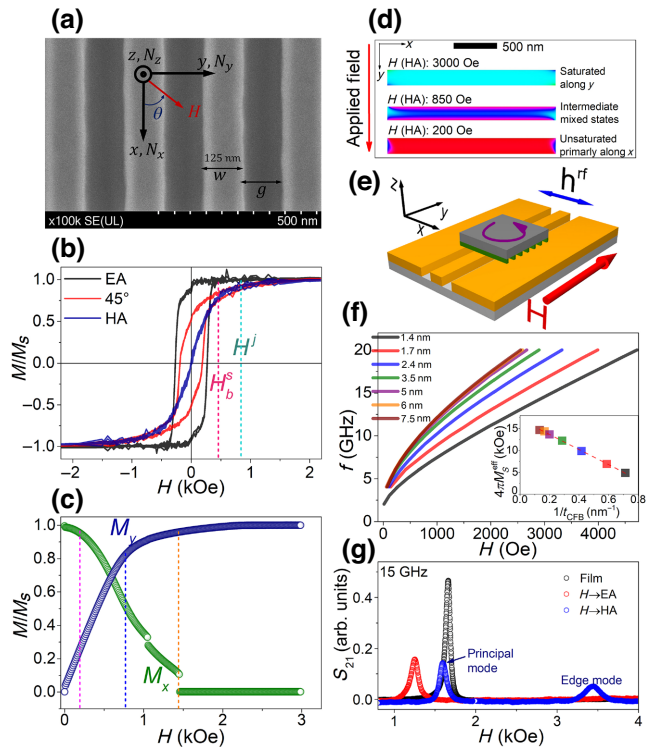


FIG. 1. (a) Typical SEM image of the patterned nanowire (*w* = *g* = 125 nm) arrays. The direction of the applied field *H* and the corresponding demagnetizing factors *N_x*, *N_y*, *N_z* along *x*, *y*, and *z* axes. (b) MH loops with *H* applied along the EA (black), at 45° (red) with respect to the EA, and along the HA (blue). (c) Relative distribution of *M_x* and *M_y* of a NW (initially magnetized along EA) with field applied along HA. (d) Snapshots of the net magnetization of the NW at different applied fields, where the red (first snapshot) and cyan (third snapshot) colors indicate the magnetizations along the *x* and *y* axes, respectively, and other colors denote the intermediate in-plane magnetizations. (e) Schematic illustration of inductive FMR using co-planar waveguide and in-plane bias field while the sample positioning is “flip-chip” type. (f) The field-frequency profiles for W(5 nm)/CFB(*t*)/MgO(2 nm) films with various *t*_{CFB} in the sub-10-nm regime. The inset shows the variation of extracted *M_s^{eff}* as a function of *t*_{CFB}. (g) Comparison of typical FMR absorption curve for the film (black) and nanowire ensembles when the bias field *H* is applied along the easy (red) and hard (blue) axis.

face down [Fig. 1(e)]. The lithographically patterned NWs (green) were placed upside down (flip chip) on top of a CPW (yellow). The bias field *H* was applied along the sample substrate plane, transverse (*y*-axis) to the microwave field (*x*-axis). Transmitted power *S₂₁* was acquired in contentious wave (CW) mode for a set of microwave frequencies (*f*) in the range of 2–20 GHz at an increment of ≤ 0.25 GHz for each set of sweep in the field range of ± 5 kOe.

C. Micromagnetic simulations

Three-dimensional micromagnetic simulations were performed using the Object Oriented Micromagnetic Framework (OOMMF) package [29]. For simulations, we have considered a single NW of length 2 μm and width 125 nm. For the angle-dependent magnetization dynamics study, we have considered the film thickness to be 6 nm (following the experimental parameter). The entire volume of the NW was discretized with cuboidal meshes of individual volume $5 \times 5 \times 3 \text{ nm}^3$. The input parameters include the saturation magnetization $M_s = 1200 \text{ emu/cm}^3$, exchange constant $A = 1.1 \text{ } \mu\text{erg/cm}$, and zero magnetocrystalline anisotropy with a damping constant $\alpha = 0.01$. The parameters were chosen from the previous publication, modeling a similar material system [30–32]. See Supplemental Material [33] for additional details on the micromagnetic simulations.

III. RESULTS AND DISCUSSION

A. Magnetometry and dynamics studies

Magnetometry results of the nanowire ensembles are presented in Fig. 1(b) using a representative sample W(5 nm)/CFB(6 nm)/MgO(2 nm), for H along the EA, 45° with respect to EA, and HA. The hysteresis loops shrink, and the effective coercive field reduces as H moves from EA to HA. A few different field regimes indicated as H_b^s , H^j as identified from the MH loops (pink and cyan dashes), are found to be critical in the dynamics, which are discussed later. The static magnetization M_x and M_y , as a function of transverse (along HA) field, as studied using micromagnetic simulations, is presented in Fig. 1(c). Three pivotal field regimes (pink, blue, and orange dashes) are identified and the corresponding magnetization profiles are depicted in Fig. 1(d). At a comparatively small transverse field (200 Oe), M_x is large (red contrast) indicating the magnetization lies mostly along the EA (x direction) of the NWs. M_y increases with a sharp decrease of M_x with increasing H . An indistinct bulk saturation field (H^j) can be identified around 850 Oe where the central region of the NW is nearly saturated along the transverse direction with a significant component of unsaturated magnetization observed near both the edges. This is due to the strong magnetostatic interaction near the NW edges due to magnetic field line closures. The edge saturation field ($H_{\text{sat}}^{\text{edge}}$) is much higher, as indicated by the orange dashed line. Spins at the edges start aligning along H beyond $H \geq H^j$ and saturation is attained (negligible M_x) around 1.5 kOe. The snapshot of magnetization at 3 kOe (cyan contrast), confirms the complete saturation of the NW along the HA.

The typical film-level FMR absorption spectra have a Lorentzian line shape, with the line position being the FMR resonance field. These resonance fields obtained for several CFB film thicknesses are plotted versus microwave

frequency f as presented in Fig. 1(f). At this ultrathin regime, the resonance frequency varies significantly with the FM layer thickness as we observe a redshift of resonance frequency with reducing t_{CFB} [34]. We fit these lines using the Kittel relation [35]:

$$f = \frac{|\gamma|}{2\pi} [(H + 4\pi M_S^{\text{eff}})(H)]^{1/2}. \quad (1)$$

From the fits the effective saturation magnetization M_S^{eff} are quantified and plotted versus $1/t_{\text{CFB}}$ [inset of Fig. 1(f)], which shows a linear variation. This size effect is seen in the form $4\pi M_S^{\text{eff}} = 4\pi M_S - (2K_S/M_S) t_{\text{CFB}}^{-1}$, and fitted to quantify $M_S(1360 \pm 60 \text{ emu/cm}^3)$ and the surface anisotropy $K_S(1.17 \pm 0.15 \text{ erg/cm}^2)$ [36]. Note that $M_S(1450 \pm 80 \text{ emu/cm}^3)$ obtained directly using magnetometry (SQUID) studies has some discrepancy with the same obtained from FMR studies. This is understood based on the fact that the fit is done using data points only up to 7.5 nm, and the inclusion of a few thicker samples could have resulted in much closer agreement.

Comparative FMR spectra obtained at 15 GHz are depicted in Fig. 1(g) for the representative sample W(5 nm)/CFB(6 nm)/MgO(2 nm) in the form of (i) continuous thin film (black circles), and (ii) nanowire arrays ($w = g \approx 125 \text{ nm}$) with H applied along the EA (blue circles) and HA (red circles). The bulk film and NW easy-axis (EA) spectra show one principal oscillation mode with resonance fields of 1670 and 1260 Oe, respectively. While the hard-axis (HA) spectra show an additional excitation around 3450 Oe beside the principal mode around 1605 Oe. This additional excitation is attributed to the inhomogeneous magnetostatic fields, localizing the magnetization precession near the edges in the HA configuration [37] and commonly known as “edge” mode [38]. Traditionally, “edge” modes are treated as a repercussion of spin-wave propagation in Damon-Eshbach (DE) configuration where H is applied transverse to the wave vector (k), which is satisfied along the HA of the NWs in the present experimental geometry. In contrast, the EA configuration is used to study the backward volume magnetostatic spin-wave (BVMSW) modes with H parallel to k [37,39,40]. While both configurations reserve fascinating fundamental physics, their intermediate geometrical configurations have rarely been reported. Such configurations could potentially contain useful information on spin-wave confinement, the origin of the “edge” mode, and in general, the evolution of the dynamics in the transition regime [41,42], which are addressed in the next section.

B. Evolution of unique nonuniform modes

A systematic angular dependence FMR spectroscopy with ultrahigh resolution, by sweeping dc field H in tiny steps (<5 Oe), is performed to address the aforementioned queries. The scan is repeated with 0.25 GHz

from 2 to 20 GHz. The raw curves are stacked together to develop the field-frequency dynamic profile capturing excitations of various relative intensities in the high-resolution two-dimensional (2D) color map form. The results presented in Fig. 2(a), for a few selective applied field angles of our interest using the representative NW [W(5 nm)/CFB(6 nm)/MgO(2 nm)]. Figure 2(a) shows the experimental profile, where the brightness represents the resonance excitation. Figure 2(b) shows the simulated ones, where the depth of red color epitomizes the resonance excitations in a gray background. For further insight, the space-frequency-resolved 2D mode profiles are depicted in Fig. 2(c), which corresponds to a few specifically selected resonance states [labeled and indicated using cross symbols in Fig. 2(b)]. It is worth mentioning that we have continued the simulations for magnetization dynamics considering a single NW, which shows a small difference in comparison with the study carried out using an assembly of five NWs. For example, the resonance frequencies for principal modes show about 1.3% difference along the easy-axis and 2.7% along the hard-axis directions. Moreover, the variation in simulated resonance frequency as a function of g indicates negligible magnetostatic interactions with $g \geq 125$ nm (see Supplemental Material [33]). Note that, we have chosen qualitatively similar states (mode) for a reasonable comparative understanding of the simulated and experimental dynamic profiles. This is because we find that similar states (modes) occur at different applied field angles for experiments and simulations as presented. Note that the experimental results are shown for the complete cycle from $+H_{\text{sat}}$ to $-H_{\text{sat}}$ whereas the simulated results are presented for half cycle, $+H_{\text{sat}}$ to $H = 0$, without losing any vital information. To comprehend the salient features of the angular-dependent dynamic spectra, we follow the field sweep protocol that begins above $+H_{\text{sat}}$ and ends beyond $-H_{\text{sat}}$. The dynamic profile along the EA of the sample is in harmony with the film level spectra, especially at a higher field-frequency regime, with one bright principal (Kittel) mode. However, it is continuous and asymmetric at lower fields across $H = 0$ [Fig. 2(a), top], unlike the film spectra. This principle mode with field applied along the EA ($H_x = H$) is seen as

$$f|_{\text{principal}}^{\text{EA}} = \frac{|\gamma|}{2\pi} \left[(H_x + N_{zx}4\pi M_S - \frac{2K_S}{t_{\text{FM}}M_S})(H_x + N_{yx}4\pi M_S) \right]^{1/2}, \quad (2)$$

which is derived from the generalized ferromagnetic resonance equation [35,43–45], and extending it for the ultrathin regime where the anisotropy $2K_S/t_{\text{FM}}$ becomes useful. $N_{zx} = N_z - N_x$ and $N_{yx} = N_y - N_x$ are the differential demagnetization factors. The frequency decreases as long as $H_x > N_{yx}4\pi M_S$, whereas for $H_x < N_{yx}4\pi M_S$ the

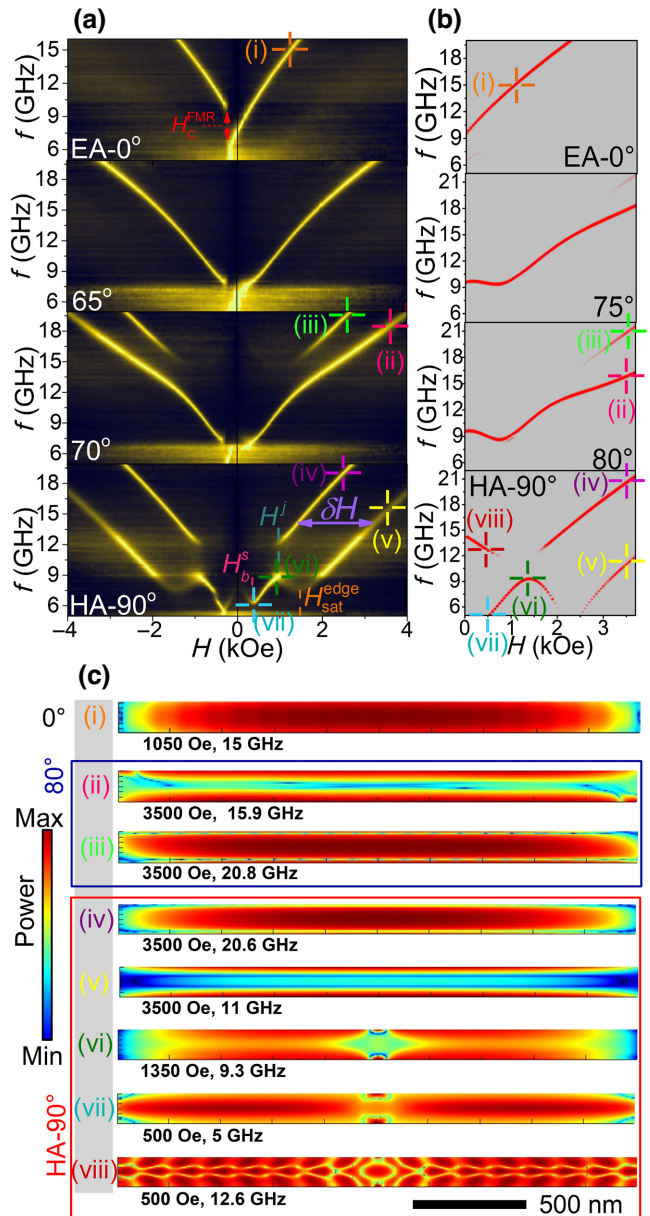


FIG. 2. Field-frequency dynamics in the 2D color plot for a few selective applied field angles with respect to the EA of the NW as obtained (a) experimentally at $0^\circ, 65^\circ, 70^\circ, 90^\circ$, and (b) using micromagnetic simulations at $0^\circ, 75^\circ, 80^\circ, 90^\circ$. (c) Simulated spin-wave mode profile (power) for the NW at the resonance frequency corresponding to the specified magnitude and direction of the applied magnetic fields. The point of interest is shown with symbols in the experimental and simulated profiles for better comparison and extraction of the mode profiles.

magnetization is reversed. This reversal is seen as the sharp jump around -250 Oe [Fig. 2(a)-top] denoted as H_C^{FMR} . Note that the reverse cycle $-H_{\text{sat}}$ to $+H_{\text{sat}}$ (not shown here) produces a mirror spectra across $H = 0$, which could be found in our prior work [30].

The characteristics of the dynamic spectra remain very similar at various angles below 60° with one bright principal mode of oscillation. To show the space-frequency-resolved 2D mode profile, a snapshot at {15 GHz; 1050 Oe} is presented in Fig. 2(c)-(i), which shows a uniform red color throughout the NW width and length except for the two ends. As the applied field angle increases, we observe deformation of the principal mode and the appearance of additional excitations. The threshold of this formation is found to be about 65° [Fig. 2(a)] from the experiments and about 75° from the simulated spectra [Fig. 2(b)]. The evolution of the dynamic spectra becomes more prominent as the angle increases, as confirmed by our corroborative experimental and simulation studies. We look into one such intermediate state (80° field configuration) for further probing into this [46]. We have picked two resonance states from the simulated spectra, corresponding to an applied field of 3.5 kOe, occurring at 20.8 GHz Fig. 2(c)-(iii) and 15.9 GHz Fig. 2(c)-(ii), while the experimental profile is also marked using the same colored cross correspondingly. We find that the characteristics of these two resonance modes are significantly different. The lower-frequency 15.9-GHz mode shows the edges of the NW show maximum power, while the center is close to power min, which indicates that this mode belongs primarily due to the confinement of the spin wave near the edges of the NW (“edge” mode). Whereas the higher-frequency mode at 20.8 GHz shows dark red color in the central region of the NW, indicating this to be the principal mode (Kittel mode) corresponding to uniform absorption. These findings are further established by comparing the dynamic profile of 80° to that of HA, where this evolution is completed. The spectral features are much more prominent, as seen for the 90° (HA) configuration, and the “edge” mode is understandably showing its maximum intensity. We notice that at the same H , but with (HA) configuration, the principal mode shows a slightly lower shift to 20.6 GHz Fig. 2(c)-(iv), and the edge mode shifts to 11 GHz Fig. 2(c)-(v). The increase in frequency spacing between the principal and edge modes is an obvious outcome due to the angular variation of H . We also find that none of the principal modes or the “edge” confined mode begins at the “0” applied field at HA configuration. Different threshold fields belong to these modes as denoted by H^j (light blue) and $H_{\text{sat}}^{\text{edge}}$ (orange) and subsequently indicated (light blue and orange dashed lines) in Figs. 1(b) and 1(c). The principal mode along HA configuration can be seen in the functional form as [35,43–45]:

$$f|_{\text{principal}}^{\text{HA}} = \frac{|\gamma|}{2\pi} \left[\left(H_y + N_{zy} 4\pi M_S - \frac{2K_S}{t_{\text{FM}} M_S} \right) - (H_y + N_{xy} 4\pi M_S) \right]^{1/2}. \quad (3)$$

Here $N_{zy} = N_z - N_y$ and $N_{xy} = N_x - N_y$ are the differential demagnetization factors. The HA configuration displays several distinguishable engrossing features [47,48]. We see a bright mode in the relatively small field regime around $+400$ (H_b^s) to $+950$ Oe followed by a sharp jump to a higher frequency at H^j . The MH loop of Fig. 1(b) shows that $M/M_S \sim 0.75$ at $H = +400$ Oe, and M/M_S nearly reaches saturation $H = +950$ Oe. This intermediate $+400$ Oe to $+950$ Oe field regime creates an interesting phase where the central part of the stripe is reaching saturation, and hence this mode corresponds to the unsaturated bulk magnetization of the NW. The two extreme states of this mode help us capture the mode profile from Fig. 2(c) (vi, vii), showing distinct variations in the profile along the two extremes of this mode. The sharp shift from 9 GHz to 12 GHz around $H_{\text{sat}}^{\text{edge}}$ corresponds to the transition from the unsaturated phase of the bulk magnetization of the NW to its saturated phase from which the uniform principal mode of oscillation begins. It is noted that the “edge” mode also has two phases separated by the critical field $H_{\text{sat}}^{\text{edge}}$ [38,49]. The field above $H_{\text{sat}}^{\text{edge}}$ belongs to the saturated phase of the edge magnetization and below $H_{\text{sat}}^{\text{edge}}$ down to around H^j belongs to the unsaturated phase of “edge” magnetization, which also gives rise to a nonuniform oscillation as visible in the simulated spectra. Although very weak, the traces can still be observed in the experimental spectra. The resonance frequency of this mode is found to decrease with increasing H . From the numerical model (Ref. [49]), we understand that at $H_{\text{sat}}^{\text{edge}}$, the “edge” mode frequency and M_y both go to “zero,” which is a key characteristic of the magnetic edge property. However, experimentally the “zero” frequency resonance at $H_{\text{sat}}^{\text{edge}}$ could not be observed [50] for any of our samples as elaborated in the following section.

Nonetheless, the simulated spectra show another mode in the lower-field regime below 850 Oe within the frequency range of 14.5 GHz to 12 GHz, Fig. 2(c)-(viii) which is unique (non-Kittel), showing decreasing resonance frequency with increasing applied field. The frequency of this mode can be written as $f^{\text{viii}} = (|\gamma|/2\pi) \{ (4\pi N_{yx}) [4\pi N_{zx} - (2K_S/t_{\text{FM}} M_S^2)] M_x \}^{1/2}$, where $M_x = [(M_S)^2 - (H/4\pi N_{yx})^2]^{1/2}$. The frequency vanishes for the hard-axis field $H_y = \pm 4\pi N_{yx} M_S$, and around this field, the frequency minima zone is formed for the principal mode. The space-frequency-resolved 2D mode profiles also reveal multiple standing-wave-like formations [51], which are easily distinguishable from the other mode profiles discussed so far. This mode, however, could not be cleanly detected in the experimental spectra, and we believe that it might be due to its ultralow amplitude. It is essential to mention here that the experimental observation of edge mode and a consistent trend from one sample to another requires excellent control of the lithography, fabrication, and good alignment during the dynamics

scan. Without these, the spectral features could be inconsistent or even ruined easily. Nevertheless, the excellent corroboration between the experiment and simulation results in this work has helped us to comprehend unique dynamic characteristics, and the interplay of the uniform and nonuniform oscillations, which is further extended to Damon-Eshbach (DE) configuration in the next section.

C. Influence of FM layer thicknesses on the dynamics and interplay of demagnetization factors

In this section, we investigate the role of anisotropic NW parameters governing the dynamics at the ultrathin regime using $t_{\text{CFB}} = 1.4, 1.75, 2.4, 3.5, 5, 6$, and 7 nm ; for $w (= g) = 125 \text{ nm}$. In Fig. 3(a), the HA-dynamics spectra (half-cycle only, as it is nearly symmetric across $H = 0$) for a few selective samples (t_{CFB}) are displayed, showcasing its distinctive variation as a function of the FM layer thickness. The simulated dynamic spectra, presented in Fig. 3(b), are used to corroborate the experimental findings and cover a broader thickness regime, which was not possible to cover using experiments. Simulated findings reveal that as the film thickness increases beyond 15 nm (not shown here), the principal mode gets distorted and branched into

two or more and becomes very complex for any Kittel modeling. Besides, additional modes which are weaker in magnitude, also appear at lower fields, making the dynamic spectra quite complex. Nevertheless, our experimental spectra help to identify 3.5 nm to be a critical thickness below and above which the characteristic features of the spectra are dissimilar. Fundamentally, this is caused by the relative weight of the individual demagnetization factors, which are analyzed and discussed later. We have noticed that the critical fields H^j , $H_{\text{edge}}^{\text{sat}}$ and also the separation field between the principal and “edge” mode denoted as δH have t_{CFB} dependency. For the quantification of δH , the minimum cut-off frequency is considered to be the resonance frequency at H^j as indicated by the shaded area in the central figure of Fig. 3(a). The extracted δH 's are presented in the form of a range band versus $1/t_{\text{CFB}}$ in the front panel of Fig. 3(c). δH is increasing monotonously with increasing frequency, which is depicted in the inset of Fig. 3(c). The variation of δH band versus $1/t_{\text{CFB}}$ (front panel), in this ultralow thickness regime of below 10 nm , is found to be quasilinear (shaded area) especially as the thickness approaches 1 nm . The inverse FM layer thickness dependency of δH has never been reported before.

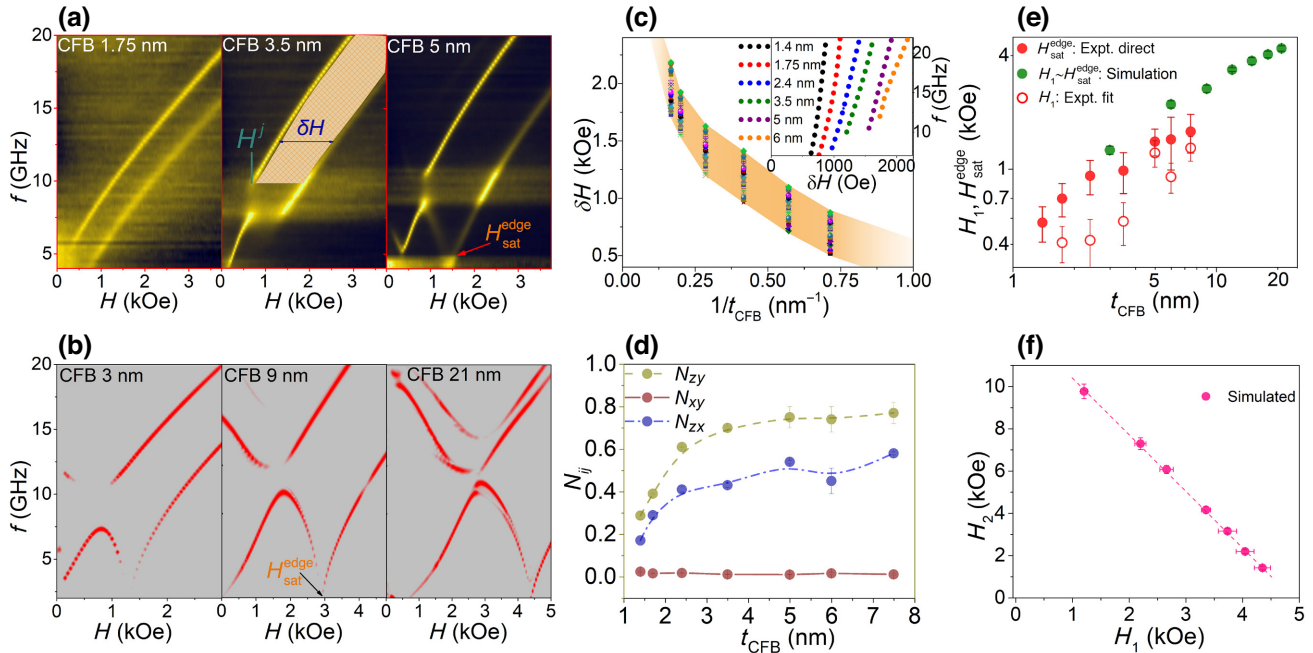


FIG. 3. Evolution of principal and edge modes as obtained (a) experimentally and (b) via micromagnetic simulations for a few selective FM layer thicknesses (experimental, $t_{\text{CFB}} = 1.75, 3.5, 5 \text{ nm}$; simulation, $t_{\text{CFB}} = 3, 9, 21 \text{ nm}$). (c) The δH as quantified from all the dynamics spectra for the various CFB thicknesses are plotted versus t_{CFB} . (d) N_{ij} (N_{zy}, N_{xy}, N_{zx}) as obtained from the fits of the principal mode (HA) are plotted versus t_{CFB} . (e) Edge saturation field $H_{\text{edge}}^{\text{sat}}$, as obtained directly from the experimental dynamic spectra (red filled circle) and for the simulated spectra as obtained using fits: $H_1 \sim H_{\text{sat}}^{\text{edge}}$ (green filled circle) are plotted versus t_{CFB} in a log-log scale. Obtained H_1 from the fits of the experimental spectra is depicted using the red hollow circle for comparison. (f) Variation of H_2 as a function of H_1 obtained from simulation data.

Further, the principal modes along HA are fitted using Eq. (3), while the “edge” modes are fitted using [49,52]

$$f|_{\text{edge}}^{\text{HA}} = \frac{|\gamma|}{2\pi} [(H_y - H_1)(H_y + H_2)]^{1/2}. \quad (4)$$

Here H_1 and H_2 are the fitting parameters, which are the combination of magnetostatic and exchange fields: $H_1 = H_{ex} + 4\pi M_S N_{yx}$, $H_2 = H_{ex} + 4\pi M_S N_{zx} - (2K_S/t_{\text{FM}}M_S)$ [49]. In the ideal scenario, $H_1 \sim H_{\text{sat}}^{\text{edge}}$ when the edge mode frequency becomes zero ($f|_{\text{edge}}^{\text{HA}} = 0$) [49,53]. Obtained differential demagnetization factors are summarized in Fig. 3(d) as a function of $1/t_{\text{CFB}}$. From 7.5 nm down to 3.5 nm we see a monotonous decrease in N_{zy} and N_{zx} . Below 3.5 nm the decrease is found to be much sharper in both of them, while N_{xy} remains negligibly small throughout this entire thickness range. From the fits of “edge” mode, the extracted H_{ex} was also found to be decreasing from 1250 Oe for 7.5 nm to 200 Oe for 1.4 nm in a quasilinear (not shown here) form. We note that by definition, $H_{\text{sat}}^{\text{edge}}$ is identified as the field where the precession frequency drops to zero. Although this relation holds fairly well for the simulated spectra leading to $H_1 \sim H_{\text{sat}}^{\text{edge}}$, we find that the intensity of the edge mode usually diminishes at a finite nonzero $f|_{\text{edge}}^{\text{HA}}$ for the experimental spectra. Using fits, we can quantify H_1 and H_2 for both the simulated and experimental dynamic profiles. Moreover, for the experimental spectra, we use the simple averaging method of a few raw curves around the diminishing intensity of the edge mode (see Supplemental Material [33]) to quantify $H_{\text{sat}}^{\text{edge}}$. In Fig. 3(e), a comparison of H_1 and $H_{\text{sat}}^{\text{edge}}$ from the experimental dynamics spectra and the same for the simulated dynamic profile are depicted versus t_{CFB} in a log-log scale. The plot shows reasonable agreement between the trends exhibited by our experimental and simulated data for $H_{\text{sat}}^{\text{edge}}$. The H_1 as extracted from the experimental dynamic profiles using fits was found to be much lower compared to $H_{\text{sat}}^{\text{edge}}$ that is directly extracted. We believe that the finite nonzero $f|_{\text{edge}}^{\text{HA}}$ is the primary reason behind this lower shift of H_1 . Note that since we have kept the separation between the NWs at 125 nm for this study, the fabrication challenges limit us from developing the sample with a much thicker FM layer. Nevertheless, our simulated spectra, which cover an extended thickness range, are found to be in excellent qualitative agreement with prior reports based on numerical calculations by McMichael *et al.* [49] using nanowires of 250-nm-wide NWs with t_{FM} between 2 to 1000 nm (see Supplemental Material [33]). Further, we have plotted H_2 versus H_1 in Fig. 3(f), obtained using the simulated spectra fits, which showcases an excellent linear variation of H_2 as a function of H_1 . However the same linearity could not be seen from the same extracted from experimental data (not shown here), which we infer to the finite nonzero $f|_{\text{edge}}^{\text{HA}}$. Most of our findings display

an excellent coherence amongst the experiments, simulations, and existing models to provide a strong ground for understanding the interplay of several anisotropic parameters of the NW that govern the dynamics, especially at the Damon-Eshbach (DE) configuration. Next, we investigate further the influence of a few other geometrical and interfacial factors on the dynamics.

D. Influence of adjacent materials and interfaces on the dynamics

Here, we probe the influence of nanowire width and the normal metal (NM)/ ferromagnet (FM) interface on the dynamics [54]. The width dependency study is carried out using micromagnetic simulation, considering NW ($t_{\text{CFB}} = 6$ nm) widths of 75, 125, 150, and 200 nm, while the length of the nanowires was kept at 2 μm to maintain a high length-to-width ratio. In Fig. 4(a), the simulated dynamic profiles are displayed, which indicates a relatively moderate impact of width variation on the nanowire ensemble dynamics within the chosen regime for width. Notably, we find that for the 75 nm, the threshold frequency for the principal mode is around 14 GHz, which comes down gradually with increasing width, which is found to be around 10 GHz for 200 nm. The edge modes are fitted using Eq. (3), which enables the qualification of H_1 , and H_2 as plotted versus w in Fig. 4(b). We have found that H_1 ($\sim H_{\text{sat}}^{\text{edge}}$) increases gradually with decreasing w . Although the range of this variation is rather small (2.17–2.32 kOe). Similarly, H_2 was found to be decreasing gradually with decreasing w and range bound within (7.15–7.4 kOe). The other low-intensity non-Kittel modes are also found to display small modulations in their curvatures upon the width variations. A similar experimental study is carried out using w : 125, 150, 200 nm for which a much thinner FM layer ($t_{\text{CFB}} = 1.4$ nm) was considered. This extremely thin layer is chosen to ensure a low value of N_{zy} (as discussed above) so that the interplay of N_x , N_y , and N_z is minimum, and the impact of the wire width could become maximum. The principal and the “edge” modes are extracted for each of the five sets of samples and stacked together for comparison; as depicted on the left part of Fig. 4(c), while the corresponding δH ’s are shown on the right part of Fig. 4(c). Extracted anisotropic fields are plotted in Fig. 4(d) versus w . Note that the FM layer thickness used for simulation and the experiment (deliberately) was quite different, allowing only a qualitative comparison among the results. We find that the variation for δH is very weakly dependent on w , and also the range of variation for $H_{\text{sat}}^{\text{edge}}$ is quite narrow. The range boundedness for H_1 and H_2 still holds good, but the nature of variation versus w is not the same as what is obtained in simulations. On the other hand, the influence of the adjacent materials to the ferromagnetic layer is found to be much more compelling. To amplify any impact of the

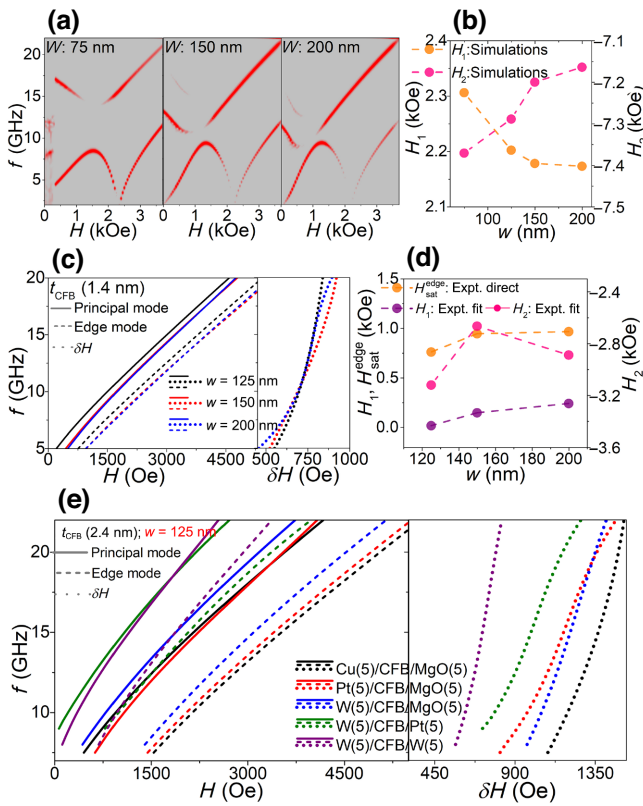


FIG. 4. (a) Simulated dynamic profiles ($t_{\text{CFB}} = 6 \text{ nm}$) for different NW widths: 75, 150, 200 nm revealing the influence of width of the dynamics. (b) The corresponding H_1 , and H_2 are plotted as a function of NW widths w . (c) Experimental dynamic profiles for different ($t_{\text{CFB}} = 1.4 \text{ nm}$) NW widths: 125 nm, 150 nm, 200 nm in compact form alongside the quantified δH . (d) The analyzed anisotropic field parameters H_1 , H_2 , and H_{Edge} are depicted as a function of NW widths w . (e) Influence of the adjacent materials of the FM layer in NM1(5 nm)/CFB(2.4 nm)/NM2(5 nm), or MgO(2 nm) stack on the dynamics. On the left, the principal and edge modes are stacked together and on the right, the corresponding quantified δH are shown.

adjacent NM layer on the dynamics without losing much of the signal-to-noise in our spectrum, we have chosen a slightly thicker CFB layer for this study in a series of samples: NM1(5 nm)/CFB(2.4 nm)/NM2(5 nm) or MgO(2 nm), while keeping the nanowire width 125 nm. The results of such five different compositions, as summarized in Fig. 4(e). The principal and the “edge” modes are extracted for each of the five sets of samples and stacked together for comparison; as depicted on the left part of Fig. 4(e), while the corresponding δH 's are shown on the right part of Fig. 4(e). We find that the principal mode, “edge” mode, and the δH are heavily influenced by the adjacent material of the ferromagnetic layer. We see that the heavier metal (W) shifts both the principal and the “edge” mode towards the lower field. The same impact is much more pronounced as we move

from NM1/FM/MgO to NM1/FM/NM2. Moreover, a closer look at the f versus δH plot helps us to resolve the impact with a greater degree. The curve for the Cu(5 nm)/CFB(2.4 nm)/MgO(2 nm) sample, which supposedly has the least interface anisotropy and no other effects like interfacial DMI, lies at a higher field. The introduction of heavy metals like W and Pt on one side of CFB pushes the line towards the left or lower fields. Upon adding the heavy metal on both sides of CFB, δH lines are pushed further towards the lower field side. These findings reveal that $H_{\text{sat}}^{\text{edge}}$ is not just a function of FM layer thickness; the adjacent materials or interface can heavily influence it, especially in the ultrathin ferromagnetic regime, a characteristic that could be useful for the design [55,56] of nanowire-based magnonics applications [57,58].

IV. CONCLUSION

Using experiments and micromagnetic simulations, we have probed the spin-wave dynamics of nanowire ensembles in ultrathin ferromagnetic limits, which exhibit several intriguing features. The dynamics in general and the evolution of the edge mode in the transition regime between BVMSW and DE configuration display unforeseen transition of the dynamic spectra (around 70° – 80° of applied field angle) and not a gradual one, where geometrical factors like thickness and width play a pivotal role. The spatial mapping of magnetization evinces unique spin distribution, giving rise to fascinating spectral patterns depending on the interplay amongst the field, frequency, and the applied field angle. At the ultrathin limits, the dynamics are heavily influenced by magnetic layer thickness (t_{CFB}). We find that there is a critical $t_{\text{CFB}} \sim 3 \text{ nm}$, below and above which the dynamic characteristics alter, which could be understood based on the interplay of the different demagnetization factors N_x , N_y , N_z . Critical entities such as field separation δH between uniform to edge mode show an inverse correlation with t_{CFB} , while the edge saturation field $H_{\text{sat}}^{\text{edge}}$ shows a linear increase with t_{CFB} in a log-log scale. The experimental findings commensurate very well with micromagnetic simulations and both are in line with prior numerical model [44,45,49]. Under the scenario where dipolar exchange is minimum, parameters such as the NW width and separation were found to have minimal impact on the edge mode and, in general, on the dynamics of nanowire ensembles. Our results show that the adjacent metals of the ferromagnet at these ultrathin limits influence the dynamics by introducing additional anisotropy from the interface or the interfacial DMI's, which can be different for non identical NM-FM pairs [59]. With a lower thickness-to-width aspect ratio than the nanowires, this influence could be magnified and can be used as a tool to tailor the characteristics [32] that are useful for applications purpose [60]. Our findings over a range of

geometrical parameters and for two fundamentally different systems offer a range of information and understanding and have fundamental [59,61] and technical significance [62–64]. This also provides a platform for tuning and controlling static and dynamic properties by geometry design and exploring alternative materials and structures [65–67] for future microwave-based applications [62–64]. Recent reports [68] on the Chiral coupling between the nanomagnets that are separated beyond dipolar exchange limits could propel further development of this field.

ACKNOWLEDGMENT

This work is funded by the SpOT-LITE programme (A*STAR Grant No. A18A6b0057) through RIE2020 funds and A*STAR core fund (TMR190715aIMRASF) from Singapore.

- [1] M. Krawczyk and D. Grundler, Review and prospects of magnonic crystals and devices with reprogrammable band structure, *J. Phys.: Condens. Matter* **26**, 123202 (2014).
- [2] A. V. Chumak, V. I. Vasyuchka, A. A. Serga, and B. Hillebrands, Magnon spintronics, *Nat. Phys.* **11**, 453 (2015).
- [3] A. V. Chumak, A. A. Serga, and B. Hillebrands, Magnonic crystals for data processing, *J. Phys. D: Appl. Phys.* **50**, 244001 (2017).
- [4] M. P. Kostylev, G. Gubbiotti, J.-G. Hu, G. Carlotti, T. Ono, and R. L. Stamps, Dipole-exchange propagating spin-wave modes in metallic ferromagnetic stripes, *Phys. Rev. B* **76**, 054422 (2007).
- [5] Ki-Suk Lee, Dong-Soo Han, and Sang-Koog Kim, Physical origin and generic control of magnonic band gaps of dipole-exchange spin waves in width-modulated nanostrip waveguides, *Phys. Rev. Lett.* **102**, 127202 (2009).
- [6] Marc Vogel, Rick Abmann, Philipp Pirro, Andrii V. Chumak, Burkard Hillebrands, and Georg von Freymann, Control of spin-wave propagation using magnetisation gradients, *Sci. Rep.* **8**, 11099 (2018).
- [7] Liang-Juan Chang, Jilei Chen, Danru Qu, Li-Zai Tsai, Yen-Fu Liu, Ming-Yi Kao, Jun-Zhi Liang, Tsuei-Shin Wu, Tien-Ming Chuang, Haiming Yu, and Shang-Fan Lee, Spin wave injection and propagation in a magnetic nanochannel from a vortex core, *Nano Lett.* **20**, 3140 (2020).
- [8] Jesco Topp, Jan Podbielski, Detlef Heitmann, and Dirk Grundler, Formation and control of internal spin-wave channels in arrays of densely packed permalloy nanowires, *J. Appl. Phys.* **105**, 07D302 (2009).
- [9] Z. K. Wang, V. L. Zhang, H. S. Lim, S. C. Ng, M. H. Kuok, S. Jain, and A. O. Adeyeye, Observation of frequency band gaps in a one-dimensional nanostructured magnonic crystal, *Appl. Phys. Lett.* **94**, 083112 (2009).
- [10] J. Ding, M. Kostylev, and A. O. Adeyeye, Magnetic hysteresis of dynamic response of one-dimensional magnonic crystals consisting of homogenous and alternating width nanowires observed with broadband ferromagnetic resonance, *Phys. Rev. B* **84**, 054425 (2011).
- [11] K. Di, S. X. Feng, S. N. Piramanayagam, V. L. Zhang, H. S. Lim, S. C. Ng, and M. H. Kuok, Enhancement of spin-wave nonreciprocity in magnonic crystals via synthetic antiferromagnetic coupling, *Sci. Rep.* **5**, 1 (2015).
- [12] J. Ding, V. E. Demidov, M. G. Cottam, S. O. Demokritov, and A. O. Adeyeye, Dynamic behavior of Ni₈₀Fe₂₀ nanowires with controlled defects, *Appl. Phys. Lett.* **104**, 143105 (2014).
- [13] Wei Tang, Zhen-wei Zhou, Yao-zhuang Nie, Qing-lin Xia, Zhong-ming Zeng, and Guang-hua Guo, Spin wave modes of width modulated Ni₈₀Fe₂₀/pt nanostrip detected by spin-orbit torque induced ferromagnetic resonance, *Appl. Phys. Lett.* **111**, 172407 (2017).
- [14] A. A. Serga, A. V. Chumak, and B. Hillebrands, YIG magnonics, *J. Phys. D: Appl. Phys.* **43**, 264002 (2010).
- [15] V. D. Bessonov, M. Mruczkiewicz, R. Gieniusz, U. Guzowska, A. Maziewski, A. I. Stognij, and M. Krawczyk, Magnonic band gaps in YIG-based one-dimensional magnonic crystals: An array of grooves versus an array of metallic stripes, *Phys. Rev. B* **91**, 104421 (2015).
- [16] G. Gubbiotti, S. Tacchi, M. Madami, G. Carlotti, Z. Yang, J. Ding, A. O. Adeyeye, and M. Kostylev, Collective spin excitations in bicomponent magnonic crystals consisting of bilayer permalloy/Fe nanowires, *Phys. Rev. B* **93**, 184411 (2016).
- [17] L. L. Xiong and A. O. Adeyeye, Dynamic behavior of Ni₈₀Fe₂₀ nanowires with controlled periodic width modulation, *Appl. Phys. Lett.* **108**, 262401 (2016).
- [18] Robert D. McMichael, C. A. Ross, and Vivian P. Chuang, Thickness dependence of magnetic film edge properties in Ni₈₀Fe₂₀ stripes, *J. Appl. Phys.* **103**, 07C505 (2008).
- [19] Z. K. Wang, V. L. Zhang, H. S. Lim, S. C. Ng, M. H. Kuok, S. Jain, and A. O. Adeyeye, Nanostructured magnonic crystals with size-tunable bandgaps, *ACS Nano* **4**, 643 (2010).
- [20] Fusheng Ma and Yan Zhou, Interfacial Dzialoshinskii–Moriya interaction induced nonreciprocity of spin waves in magnonic waveguides, *RSC Adv.* **4**, 46454 (2014).
- [21] Benjamin W. Zingsem, Michael Farle, Robert L. Stamps, and Robert E. Camley, Unusual nature of confined modes in a chiral system: Directional transport in standing waves, *Phys. Rev. B* **99**, 214429 (2019).
- [22] S. Pile, T. Feggeler, T. Schaffers, R. Meckenstock, M. Buchner, D. Spoddig, B. Zingsem, V. Ney, M. Farle, H. Wende, H. Ohldag, A. Ney, and K. Ollefs, Non-standing spin-waves in confined micrometer-sized ferromagnetic structures under uniform excitation, *Appl. Phys. Lett.* **116**, 072401 (2020).
- [23] S. Tacchi, G. Gubbiotti, M. Madami, and G. Carlotti, Brillouin light scattering studies of 2D magnonic crystals, *J. Phys.: Condens. Matter* **29**, 073001 (2016).
- [24] Changting Dai, Kaile Xie, Zizhao Pan, and Fusheng Ma, Strong coupling between magnons confined in a single magnonic cavity, *J. Appl. Phys.* **127**, 203902 (2020).
- [25] Maxim Goryachev, Warrick G. Farr, Daniel L. Creedon, Yaohui Fan, Mikhail Kostylev, and Michael E. Tobar, High-cooperativity cavity QED with magnons at microwave frequencies, *Phys. Rev. Appl.* **2**, 054002 (2014).
- [26] Sergi Lendinez, Mojtaba T. Kaffash, and M. Benjamin Jungfleisch, Emergent spin dynamics enabled by lattice

- interactions in a bicomponent artificial spin ice, *Nano Lett.* **21**, 1921 (2021).
- [27] Shikun He and Christos Panagopoulos, A broadband ferromagnetic resonance dipper probe for magnetic damping measurements from 4.2 K to 300 K a broadband ferromagnetic resonance dipper probe for magnetic damping measurements from 4.2 K to 300 K, *Rev. Sci. Instrum.* **87**, 043110 (2016).
- [28] S. Gupta, R. Sbiaa, M. Al Bahri, A. Ghosh, S. N. Piramanayagam, M. Ranjbar, and J. Akerman, [Co/Ni] multilayers with robust post-annealing performance for spintronics device applications, *J. Phys. D: Appl. Phys.* **51**, 465002 (2018).
- [29] M. Donahue and D. G. Porter, *OOMMF User's Guide, Version 1.0, Interagency Report NISTIR 6376* (National Institute of Standard and Technology, Gaithersburg, MD), <http://math.nist.gov/oommf>.
- [30] Abhijit Ghosh, Fusheng Ma, James Lourembam, Xiangjun Jin, Ramu Maddu, Qi Jia Yap, and Sze Ter Lim, Emergent dynamics of artificial spin-ice lattice based on an ultrathin ferromagnet, *Nano Lett.* **20**, 109 (2020).
- [31] A. Talapatra, N. Singh, and A. O. Adeyeye, Magnetic tunability of permalloy artificial spin ice structures, *Phys. Rev. Appl.* **13**, 014034 (2020).
- [32] A. Talapatra and A. O. Adeyeye, Linear chains of nanomagnets: Engineering the effective magnetic anisotropy, *Nanoscale* **12**, 20933 (2020).
- [33] See Supplemental Material at <http://link.aps.org/supplemental/10.1103/PhysRevApplied.20.044034> for additional details on the micromagnetic simulations.
- [34] S. Gupta, D. Kumar, T. L. Jin, R. Nongjai, K. Asokan, A. Ghosh, M. Aparna Devi, P. Suri, and S. N. Piramanayagam, Broadband strip-line ferromagnetic resonance spectroscopy of soft magnetic cofetazr patterned thin films, *AIP Adv.* **8**, 056125 (2018).
- [35] Charles Kittel, On the theory of ferromagnetic resonance absorption, *Phys. Rev.* **73**, 155 (1948).
- [36] James O. Rantschler, P. J. Chen, A. S. Arrott, R. D. McMichael, W. F. Egelhoff, and B. B. Maranville, Surface anisotropy of permalloy in Nm/NiFe/Nm multilayers, *J. Appl. Phys.* **97**, 10J113 (2005).
- [37] Philipp Wessels, Andreas Vogel, Jan-Niklas Tödt, Marek Wieland, Guido Meier, and Markus Drescher, Direct observation of isolated Damon-Eshbach and backward volume spin-wave packets in ferromagnetic microstripes, *Sci. Rep.* **6**, 22117 (2016).
- [38] B. B. Maranville, R. D. McMichael, S. A. Kim, W. L. Johnson, C. A. Ross, and Joy Y. Cheng, Characterization of magnetic properties at edges by edge-mode dynamics, *J. Appl. Phys.* **99**, 08C703 (2006).
- [39] Vladislav E. Demidov, Sergei Urazhdin, Ronghua Liu, Boris Divinskiy, Andrey Telegin, and Sergej O. Demokritov, Excitation of coherent propagating spin waves by pure spin currents, *Nat. Commun.* **7**, 1 (2016).
- [40] M. Evelt, L. Soumah, A. B. Rinkevich, S. O. Demokritov, A. Anane, V. Cros, Jamal Ben Youssef, G. de Loubens, O. Klein, P. Bortolotti, and V. E. Demidov, Emission of coherent propagating magnons by insulator-based spin-orbit-torque oscillators, *Phys. Rev. Appl.* **10**, 041002 (2018).
- [41] M. Kostylev, P. Schrader, R. L. Stamps, G. Gubbiotti, G. Carlotti, A. O. Adeyeye, S. Goolaup, and N. Singh, Partial frequency band gap in one-dimensional magnonic crystals, *Appl. Phys. Lett.* **92**, 132504 (2008).
- [42] Susmita Saha, Saswati Barman, YoshiChika Otani, and Anjan Barman, All-optical investigation of tunable picosecond magnetization dynamics in ferromagnetic nanostripes with a width down to 50nm, *Nanoscale* **7**, 18312 (2015).
- [43] Amikam Aharoni, Demagnetizing factors for rectangular ferromagnetic prisms, *J. Appl. Phys.* **83**, 3432 (1998).
- [44] Osamu Kohmoto, Effective demagnetizing factors in ferromagnetic resonance equations, *J. Magn. Magn. Mater.* **262**, 280 (2003).
- [45] Osamu Kohmoto, Perpendicular ferromagnetic-resonance equations derived by effective demagnetizing factors, *Jpn. J. Appl. Phys.* **42**, 7299 (2003).
- [46] Chandrima Banerjee, Samiran Choudhury, Jaivardhan Sinha, and Anjan Barman, Pseudo-one-dimensional magnonic crystals for high-frequency nanoscale devices, *Phys. Rev. Appl.* **8**, 014036 (2017).
- [47] M. Zhu and R. D. McMichael, Modification of edge mode dynamics by oxidation in Ni₈₀Fe₂₀ thin film edges, *J. Appl. Phys.* **107**, 103908 (2010).
- [48] Han-Jong Chia, Feng Guo, L. M. Belova, and R. D. McMichael, Two-dimensional spectroscopic imaging of individual ferromagnetic nanostripes, *Phys. Rev. B* **86**, 184406 (2012).
- [49] R. D. McMichael and B. B. Maranville, Edge saturation fields and dynamic edge modes in ideal and nonideal magnetic film edges, *Phys. Rev. B* **74**, 024424 (2006).
- [50] Y. Li, G. Gubbiotti, F. Casoli, F. J. T. Gonçalves, S. A. Morley, M. C. Rosamond, E. H. Linfield, C. H. Marrows, S. McVitie, and R. L. Stamps, Brillouin light scattering study of magnetic-element normal modes in a square artificial spin ice geometry, *J. Phys. D: Appl. Phys.* **50**, 015003 (2016).
- [51] M. Mruczkiewicz, M. Krawczyk, V. K. Sakharov, Yu. V. Khivintsev, Yu. A. Filimonov, and S. A. Nikitov, Standing spin waves in magnonic crystals, *J. Appl. Phys.* **113**, 093908 (2013).
- [52] Jaehun Cho, Yuya Fujii, Katsunori Konioshi, Jungbum Yoon, Nam-Hui Kim, Jinyong Jung, Shinji Miwa, Myung-Hwa Jung, Yoshishige Suzuki, and Chun-Yeol You, Study of spin dynamics and damping on the magnetic nanowire arrays with various nanowire widths, *J. Magn. Magn. Mater.* **409**, 99 (2016).
- [53] Brian B. Maranville, Robert D. McMichael, and David W. Abraham, Variation of thin film edge magnetic properties with patterning process conditions in Ni₈₀Fe₂₀ stripes, *Appl. Phys. Lett.* **90**, 232504 (2007).
- [54] Samiran Choudhury, Susmita Saha, Ruma Mandal, Saswati Barman, YoshiChika Otani, and Anjan Barman, Shape- and interface-induced control of spin dynamics of two-dimensional bicomponent magnonic crystals, *ACS Appl. Mater. Interfaces* **8**, 18339 (2016).
- [55] S. Atalay, A. O. Kaya, V. S. Kolat, H. Gencer, and T. Izgi, One-dimensional magnonic crystal for magnetic field sensing, *J. Supercond. Novel Magn.* **28**, 2071 (2015).
- [56] Taichi Goto, Kei Shimada, Yuichi Nakamura, Hironaga Uchida, and Mitsuteru Inoue, One-dimensional magnonic

- crystal with Cu stripes for forward volume spin waves, *Phys. Rev. Appl.* **11**, 014033 (2019).
- [57] Sebastian Gliga, Ezio Iacocca, and Olle G. Heinonen, Dynamics of reconfigurable artificial spin ice: Toward magnonic functional materials, *APL Mater.* **8**, 040911 (2020).
- [58] Frank Heussner, Giacomo Talmelli, Moritz Geilen, Björn Heinz, Thomas Brächer, Thomas Meyer, Florin Ciubotaru, Christoph Adelmann, Kei Yamamoto, Alexander A. Serga, Burkard Hillebrands, and Philipp Pirro, Experimental realization of a passive gigahertz frequency-division demultiplexer for magnonic logic networks, *Phys. Status Solidi RRL* **14**, 1900695 (2020).
- [59] M. Mruczkiewicz and M. Krawczyk, Influence of the Dzyaloshinskii-Moriya interaction on the FMR spectrum of magnonic crystals and confined structures, *Phys. Rev. B* **94**, 024434 (2016).
- [60] J. De La Torre Medina, J. Spiegel, M. Darques, L. Piraux, and I. Huynen, Differential phase shift in nonreciprocal microstrip lines on magnetic nanowired substrates, *Appl. Phys. Lett.* **96**, 072508 (2010).
- [61] Fusheng Ma, Yan Zhou, H. B. Braun, and W. S. Lew, Skyrmion-based dynamic magnonic crystal, *Nano Lett.* **15**, 4029 (2015).
- [62] Aimad Saib, Michaël Darques, Luc Piraux, Danielle Vanhoenacker-Janvier, and Isabelle Huynen, Unbiased microwave circulator based on ferromagnetic nanowires arrays of tunable magnetization state, *J. Phys. D: Appl. Phys.* **38**, 2759 (2005).
- [63] M. Darques, J. De la Torre Medina, L. Piraux, L. Cagnon, and I. Huynen, Microwave circulator based on ferromagnetic nanowires in an alumina template, *Nanotechnology* **21**, 145208 (2010).
- [64] Vivien Van Kerckhoven, Luc Piraux, and Isabelle Huynen, Substrate integrated waveguide isolator based on ferromagnetic nanowires in porous alumina template, *Appl. Phys. Lett.* **105**, 183107 (2014).
- [65] M. T. Niemier, G. H. Bernstein, G. Csaba, A. Dingler, X. S. Hu, S. Kurtz, S. Liu, J. Nahas, W. Porod, M. Siddiq, and E. Varga, Nanomagnet logic: Progress toward system-level integration, *J. Phys.: Condens. Matter* **23**, 493202 (2011).
- [66] Frank Heussner, Matthias Nabinger, Tobias Fischer, Thomas Brächer, Alexander A. Serga, Burkard Hillebrands, and Philipp Pirro, Frequency-division multiplexing in magnonic logic networks based on caustic-like spin-wave beams, *Phys. Status Solidi RRL* **12**, 1800409 (2018).
- [67] H. Arava, N. Leo, D. Schildknecht, J. Cui, J. Vijayakumar, P. M. Derlet, A. Kleibert, and L. J. Heyderman, Engineering relaxation pathways in building blocks of artificial spin ice for computation, *Phys. Rev. Appl.* **11**, 054086 (2019).
- [68] Zhaochu Luo, Trong Phuong Dao, Aleš Hrabec, Jaianth Vijayakumar, Armin Kleibert, Manuel Baumgartner, Eugenie Kirk, Jizhai Cui, Tatiana Savchenko, Gunasheel Krishnaswamy, Laura J. Heyderman, and Pietro Gambardella, Chirally coupled nanomagnets, *Science* **363**, 1435 (2019).